ADVANCED FUNCTIONAL MATERIALS
www.afm-journal.de

Chemically Processed Porous V_2O_5 Thin-Film Cathodes for High-Performance Thin-film Zn-Ion Batteries

Jingli Luo, Mengjue Cao, Nibagani Naresh, Jnanraj Borah, Shuhui Li, Tianlei Wang, Bimal K. Sarma, Jianfeng Yao, Ivan P. Parkin, and Buddha Deka Boruah**

Thin-film rechargeable batteries have a wide range of applications due to their unique properties such as small size, thinness, and the ability to power smart devices, including portable electronic devices, medical devices, smart cards, RFID tags, and Internet of Things (IoT) devices. Processing thin-film electrodes for these batteries generally relies on standard physical vapor deposition technologies. However, producing porous thin-films using these techniques presents significant challenges. Here, a rapid and cost-effective chemical route for processing porous vanadium oxide (V_2O_5) thin-film cathodes for application in Zinc-ion-based thin-film batteries (Zn-TFBs) is explored. The V_2O_5 precursor process uses an industrially viable spraying technique, which not only offers impressive charge storage performance of an areal capacity of 47.34 µAh cm^{-2}, areal energy of 50.18 µWh cm^{-2}, and areal power of 53 µW cm^{-2} at 50 µA cm^{-2} in the optimized gel-electrolyte composition. This study introduces a cost-effective and industrially viable method for processing highly porous thin-film cathodes, enabling the production of high-performance, affordable, and safer thin-film batteries.

1. Introduction

In the area of industrial 4.0, the development of IoT has changed the interaction way between individuals and the world with interconnected sensing devices.[1] Among them, fast-growing portable electronic devices, medical devices, smart cards, RFID tags, as well as wearable biosensing on wearable platforms require flexible power sources with high efficiency and sustainability.[2] Therefore, thin-film secondary batteries, with competitive energy density, stable voltage outputs and extended longevity, have been widely explored.[3] Some successful downsizing and planarization has started from rechargeable lithium-ion batteries for their high discharge voltage, satisfied energy density and stable cycle performance whereas,[3–5] the concomitant poor safety, limited reservation and fancy price impeded their further widespread in personal equipment, specifically safety is a crucial concern for wearable biosensing.[6] Therefore, alternative secondary batteries with the necessary characteristics of safer and more affordable energy storage devices are required, while also delivering sufficient energy to power the devices. Aqueous zinc-ion batteries (ZIBs) could be the ideal candidates due to their advantages, such as enhanced safety, abundant availability, economical cost, low redox voltage of zinc (−0.76 V vs SHE), and high theoretical capacity (820 mAh g^{-1}, 5855 mAh cm^{-3}). These qualities make ZIBs suitable for operation in aqueous electrolyte systems.[6,7]

The common cathode materials for ZIBs include manganese-based materials, vanadium-based materials, organic compounds, Prussian blue analogs (PBAs).[8–10] For manganese-based cathodes, the phase transition and slow reaction kinetics during charge-discharge will restrict their rate capability and cycle life.[8] For organic compounds, side reactions at zinc anode surface and product dissolution in the aqueous electrolyte will impair their capability.[11] Significant dissolution and degradation of PBAs will result in their poor cycling performance.[10] By contrast, vanadium-based materials with various stable structures and rich valence states (+5, +4, +3) have significant specific capacity (normally > 350 mAh g^{-1}), rate capability and reversibility.[6,12] Among these, V_2O_5 compounds, with their layered structure and V^{5+} valence state, offer reversible charge storage performance.

J. Luo, M. Cao, N. Naresh, B. D. Boruah
Institute for Materials Discovery
University College London (UCL)
London WC1E 7JE, UK
E-mail: b.boruah@ucl.ac.uk
J. Borah, B. K. Sarma
Department of Physics
Gauhati University
Guwahati, Assam 781014, India
S. Li, T. Wang, I. P. Parkin
Department of Chemistry
University College London (UCL)
London WC1H 0AJ, UK
E-mail: i.p.parkin@ucl.ac.uk
J. Yao
College of Chemical Engineering
Nanjing Forestry University
Nanjing 210037, China

The ORCID identification number(s) for the author(s) of this article can be found under https://doi.org/10.1002/adfm.202417607

DOI: 10.1002/adfm.202417607

Their theoretical capacity of 589 mAh g^{-1} and layered structure enable the control and tuning of capacities by expanding interlayer spacings, which facilitates Zn^{2+} insertion and extraction and further enhances cycling stability.[6,11,12] Magnetron sputtering, radio frequency magnetron sputtering, atomic layer deposition, and chemical vapor deposition are common methods for processing thin-film based oxide cathode materials.[6,13–15] However, these techniques generate coating thicknesses of less than a micrometer, leading to very low mass loading of the cathode materials. Moreover, ensuring well-aligned pores throughout remains equally challenging and can hinder continuous electrode processing.[6,14] Additionally, spray coating is a well-established industrial procedure for processing thin-films of materials. It allows for continuous, time-efficient, and cost-effective production. In addition, the development of electrolytes compatible with Zn-TFBs is equally important. Conventional aqueous electrolytes, such as 3 M $Zn(CF_3SO_3)_2$ or 2 M $ZnSO_4$ used for ZIBs, are challenging to apply directly due to potential leakage, complicating the packaging of Zn-TFBs. Hence, it is essential to explore suitable gel electrolytes, comprising these salts within specific polymer compositions, as the overall performance of Zn-TFBs is not only influenced by the cathode composition but also significantly affected by the electrolyte composition.

In this study, we explored the spraying technique to produce high-quality and porous V_2O_5 thin-films for high-performance Zn-TFBs. The porous V_2O_5 thin-film is obtained from precursors and then crystallized onto the current collectors, rather than direct spraying of V_2O_5 powder. This method ensures proper adhesion to the current collectors and achieves a binder- and conductive additive-free thin-film. The applied porous V_2O_5 thin-film, combined with a thin Zn foil as the anode and an optimized gel-electrolyte composition that eliminates the need for a separator in Zn-TFBs, delivers competitive charge storage performance. Additionally, it provides reasonably stable cycling stability and slow self-discharge capability. This study presents a method for achieving high-performance Zn-TFBs and provides guidance for developing high-performance thin-film batteries through rapid, cost-effective, and industrially viable processes.

2. Results and Discussion

The schematic diagram illustrates the process of preparing porous V_2O_5 thin-films on Ti substrates, as shown in **Figure** 1a–c. A spray solution mixture containing NH_4VO_3 and urea in HNO_3 and DI water is deposited onto cleaned Ti substrates, followed by annealing at 350 °C for 2 h. This process results in the formation of a porous V_2O_5 thin-film with well-aligned porosities. The resulting porous V_2O_5 thin-film is then used as the active material for Zn-TFBs, with the assembly process depicted in Figure 1d (details on the Zn-TFB assembly can be found in the Supporting Information). Figure 1e shows a digital image of the Zn-TFB, where Zn foil serves as the anode, and the prepared porous V_2O_5 thin-film acts as the cathode in a gel electrolyte without the use of separators. An in-depth analysis of the microstructure and morphology of the porous V_2O_5 thin-film was conducted using SEM and TEM, as shown in Figure 1f–j. The SEM image in Figure 1f reveals a nanosheet-like, well-aligned porous V_2O_5 microstructure with a film thickness of ≈13 µm (Figure 1g). The porous thin-film offers several advantages for thin-film rechargeable batteries, especially when used with gel electrolytes. The porosities facilitate effective electrolyte interaction with the electrode, increase the number of active sites and electrolyte interfaces, enhance the surface area, and allow for better diffusion of electrolyte ions, all of which contribute to improved charge storage performance. Additionally, the disordered and porous arrangement of the V_2O_5 nanosheets enhances material flexibility by releasing local stress more easily, making it an ideal cathode material for flexible Zn-TFBs. The TEM image in Figure 1h further confirms the nanosheet-like morphology of the V_2O_5, while the HRTEM analysis, indexed to orthorhombic V_2O_5, is shown in Figure 1i,j. The calculated d-spacing of 0.83 nm corresponds to the (001) plane, the most thermodynamically stable crystal plane in the V_2O_5 lattice.[16–18] The d-spacing of 0.20 nm corresponds to the (020) plane of orthorhombic V_2O_5.[19] To investigate the elemental composition of V_2O_5, TEM-based EDS was performed, as shown in Figure S1 (Supporting Information). The typical nanosheet exhibits a homogeneous distribution of V (Figure S1b, Supporting Information) and O (Figure S1c, Supporting Information) elements, indicating the successful preparation of V_2O_5.

XRD analysis was conducted to examine the crystal structure of the prepared sample, as shown in Figure 1k. The primary diffraction peaks of porous V_2O_5 on a Ti substrate, observed at 2θ values of 15.9°, 20.7°, 22.1°, 26.7°, 31.5°, 32.8°, 33.8°, 34.9°, 47.9°, and 51.8°, correspond to the (200), (001), (101), (110), (301), (011), (310), (111), (600), and (020) crystal planes of V_2O_5, respectively.[20] After excluding the Ti substrate peak, no impurity peaks were detected, indicating the successful synthesis of relatively pure V_2O_5.[20] Figure 1l shows the Raman spectra of the porous V_2O_5. The lattice bending vibration of the V—O—V bond appears at 155 cm^{-1}. Peaks at 197 and 269 cm^{-1} are attributed to the bending vibrations of the V═O and O_3—V═O bonds, respectively. The peaks at 415 and 474 cm^{-1} align with the bending vibrations of two modes of the bridging V—O—V (V—O_3—V and V—O_2—V). A peak at 524 cm^{-1} corresponds to the triple coordination oxygen stretching mode (V_3—O),[21] while the peak at 701 cm^{-1} is attributed to the doubly coordinated oxygen stretching mode (V_2—O). The characteristic bands related to the terminal V═O bond are observed at 1005 cm^{-1}.[22] Figure S1d (Supporting Information) presents the FTIR spectroscopy results for the sample. The characteristic peaks at 497 and 752 cm^{-1} correspond to the symmetric and asymmetric stretching vibrations of V—O—V in V_2O_5, respectively,[23] while the absorption peak at 1004 cm^{-1} is associated with the stretching vibration of V = O.[24] Peaks at 1615 and 1753 cm^{-1} are related to O—H bending, and the peak at 3544 cm^{-1} is attributed to O—H stretching, all of which originate from H_2O.[25] XPS was performed to determine the composition and elemental valence states (Figure 1m). Aside from signals from C, only V and O elements were detected in the survey spectrum (Figure S2, Supporting Information). The V 2p fine spectrum exhibited characteristic peaks for $V2p_{1/2}$ (524.73 eV) and $V2p_{3/2}$ (517.28 eV), corresponding solely to V^{5+} valence states,[26] indicating the high purity of the V_2O_5 phase synthesized by this method. The fitted O 1s fine spectrum shows a characteristic peak at 530.08 eV, attributed to the O signal from the V_2O_5 lattice.[27] O 1s peak occurring at 530.98 eV is ascribed to O signal from atmospheric CO_2 or H_2O.[28] According to all above, the synthesized material is proved to be V_2O_5 with high purity.

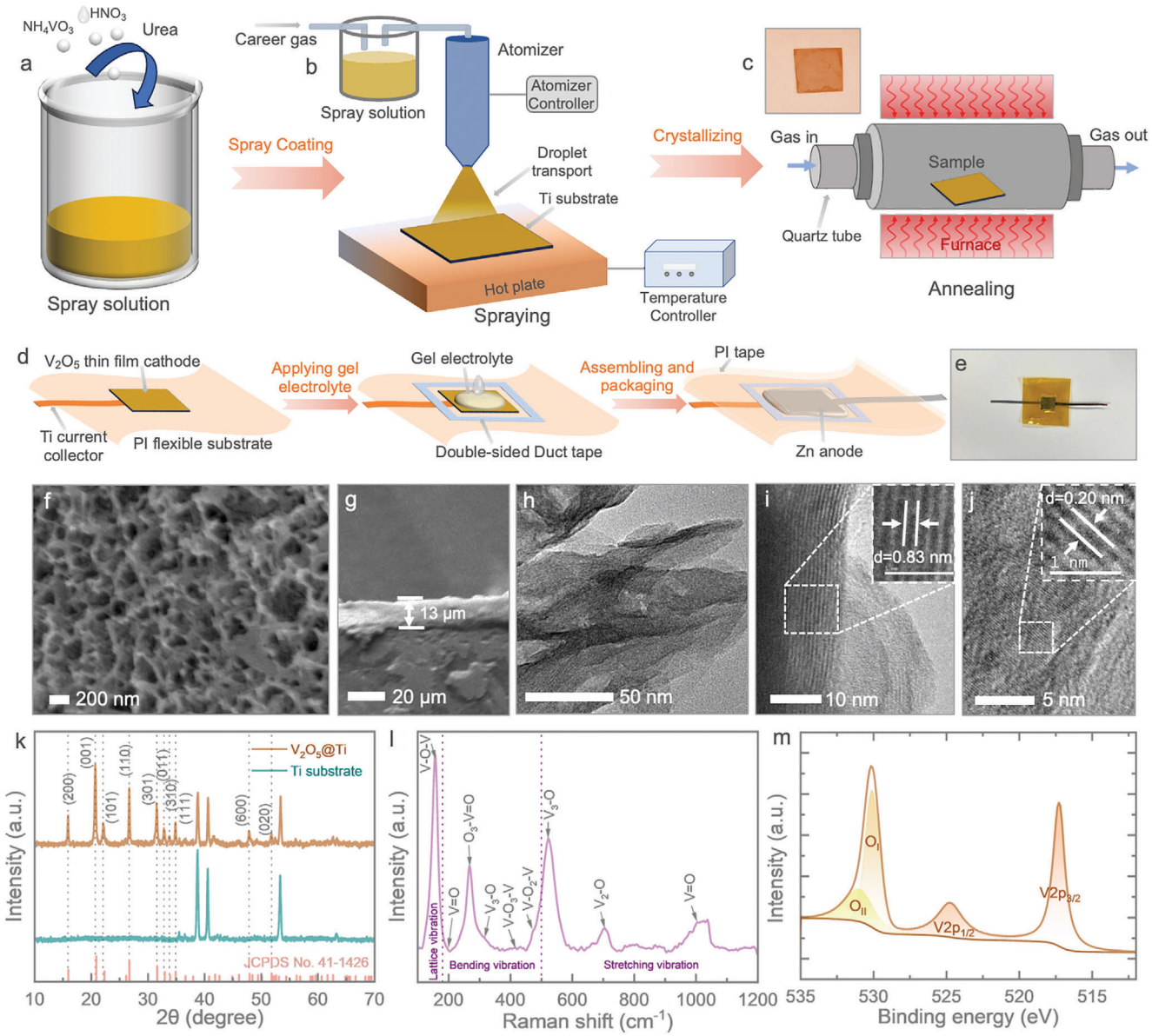

Figure 1. a–c) A schematic illustration of porous V_2O_5 on a Ti current collector, detailing the preparation of the spray solution, spraying of the solution, and crystallization of the spray-coated V_2O_5 samples. d) Schematic representation of the fabrication process for Zn-TFBs. e) A digital photograph of the assembled Zn-TFB. f,g) SEM images of the porous V_2O_5 on a Ti current collector, with a typical thickness of 13 µm. h) TEM images of porous V_2O_5. i,j) Calculation of d-spacing for respective crystal planes of V_2O_5. k) XRD patterns of porous V_2O_5 coated on a Ti substrate and bare Ti. l) Raman spectra and m) XPS high-resolution spectra for V_2O_5.

First, to evaluate the charge storage performance of the as-prepared porous V_2O_5 thin-films, we tested the cathodes by assembling coin cells and conducting tests in 3 M $Zn(CF_3SO_3)_2$ electrolyte before applying them in Zn-TFBs. Figure S3a (Supporting Information) presents the cyclic voltammetry (CV) at different scan rates ranging from 0.1 to 1.0 mV s^{-1} within a voltage range of 0.1 to 1.6 V. In all CV scans, two pairs of redox peaks are observed, for example, at 1.32/0.94 V and 1.08/0.54 V when tested at 0.1 mV s^{-1}, which correspond to the Zn^{2+} intercalation and de-intercalation processes in the V_2O_5 cathode.[13] To better understand the charge storage mechanism, we performed additional calculations to differentiate between capacitive-dominant and diffusion-dominant charge storage processes. The peak current (i_p) of the redox peaks can be expressed with scan rate (ν) according to the following relationship: $i_p = a\nu^b$, where a and b are adjustable parameters. The value of b determines the nature of the charge storage mechanism: a completely diffusion-controlled process occurs when b equals 0.5, and a capacitance-controlled process occurs when b equals 1.0.[29] To gain further insight into the charge-discharge process, the b values were calculated from the plots for the major anodic and cathodic (Figure S3b, Supporting Information) peaks. The calculated b values for the anodic and cathodic peaks are 0.74 and 0.53, respectively, indicating that the overall charge storage process is primarily

governed by diffusion-controlled mechanisms. Additionally, the charge storage process can be divided into capacitive-controlled ($k_1\nu$) and diffusion-controlled ($k_2\nu^{0.5}$) components, based on the current–voltage relation: $i(V) = k_1\nu + k_2\nu^{0.5}$; $i(V)/\nu^{0.5} = k_1\nu^{0.5} + k_2$.[30] Using this relationship, we calculated the contributions from diffusion-controlled and capacitive-controlled processes at different scan rates, as shown in Figure S3c (Supporting Information). Typically, at lower scan rates, Zn^{2+} storage is predominantly governed by diffusion mechanisms. However, as the scan rate increases from 0.1 to 1.0 mV s^{-1}, the influence of diffusion-controlled processes decreases, with its contribution reducing from 70% to 42%. Figure S3d,e (Supporting Information) presents the galvanostatic discharge-charge (GDC) tests at various specific currents and rate tests, with the calculated specific capacities of 153, 75, and 59 mAh g^{-1} at specific currents of 50, 500, and 1000 mA g^{-1}, respectively. These values exceed those reported for cathodes produced by other methods (as shown in Table S1, Supporting Information), highlighting the potential advantages of our chemically processed porous V_2O_5 thin-film cathodes for application in Zn-TFBs. We further evaluate the performance of chemically processed porous V_2O_5 thin-film cathodes and compare their electrochemical performance with that of V_2O_5 thin-film cathodes produced by sputtering. The porous V_2O_5 thin-film cathodes exhibit significantly higher areal capacitances compared to those produced by sputtering. This highlights the advantages of porous V_2O_5 thin-film cathodes, including an increased number of active sites, an enhanced electrolyte-electrode interface, greater surface area, and improved electrolyte ion diffusion (see further).

Next, we have evaluated the performance of the Zn-TFBs. Details of the fabrication process are provided in the Supporting Information. To achieve optimal electrochemical performance and capacitance stability in our Zn-TFBs, we first optimized a porous V_2O_5 thin-film cathode paired with a zinc anode by exploring various gel electrolytes. These were prepared by dissolving 3 M $Zn(CF_3SO_3)_2$ in guar gum (GG) and polyvinyl alcohol (PVA) matrices (see Figure S4, Supporting Information). The preparation details for the gel electrolytes are provided in the Supporting Information. The use of 3 M $Zn(CF_3SO_3)_2$ results in a more conductive gel electrolyte, offering much better electrochemical performance compared to 2 M $Zn(CF_3SO_3)_2$ in the same polymer matrices (see Figure S5, Supporting Information). Therefore, throughout the manuscript, we utilized 3 M $Zn(CF_3SO_3)_2$ in GG and PVA gel electrolytes, both having a similar water content of ≈47% (refer to Figure S6, Supporting Information). These electrolytes present additional advantages compared to conventional electrolytes, such as eliminating the need for a separator, simplifying the packaging of thin-film batteries by reducing leakage issues, and improving the effectiveness of the electrode and electrolyte interfaces. Figure S7 (Supporting Information) presents digital and microscopic images of Zn-TFBs, where the measured typical thickness of the electrolyte is ≈70 µm. First, we examined the CVs at different scan rates ranging from 0.1 to 1.0 mV s^{-1} over the potential range of 0.2 to 1.6 V for the Zn-TFBs using GG and PVA gels, referred to as "GG" and "PVA" throughout the manuscript. Figure S8a–d (Supporting Information) illustrates the respective CV and GDC curves of GG and PVA Zn-TFBs. The comparative CV curves for both thin-film batteries at scan rates of 0.2 and 1.0 mV s^{-1} are depicted in **Figure 2**a,b. It is evident that GG shows higher areal currents than PVA at the same scan rates. Similarly, two pairs of redox peaks at 1.21/0.89 and 0.83/0.36 V at 1.0 mV s^{-1} correspond to Zn^{2+} intercalation and de-intercalation processes in the V_2O_5 cathode.[13] For the major anodic peak (Figure 2c), the *b* value was 0.83 for GG, indicating that the charge storage process involves both capacity-controlled and diffusion-controlled processes. The *b* value for PVA was 0.49, suggesting a diffusion-controlled process. Similarly, the *b* values for the major cathodic peaks (Figure 2d) were close to 0.5, indicating diffusion-controlled charge storage. These calculations suggest that the overall charge storage mechanism in GG involves both capacitive and diffusion-controlled processes, whereas in PVA, it is purely diffusion-controlled. This implies that the GG-based electrolyte offers better charge storage kinetics and can operate at faster rates compared to the PVA electrolyte (see further details). We calculated the contributions from diffusion-controlled and capacitive-controlled processes at different scan rates for both GG and PVA, as shown in Figure 2e. In the GG Zn-TFBs, diffusion-controlled storage plays a dominant role in Zn^{2+} storage at low scan rates. As the scan rate increases, the contribution from diffusion-controlled storage decreases from 70% to 43% when the scan rate increases from 0.1 to 1.0 mV s^{-1}. The estimated capacitive current contribution is highlighted by the shaded regions in the CV profiles shown in Figure S9a,b (Supporting Information). Conversely, in the PVA-based battery, charge storage is predominantly diffusion-controlled, with 83% of charge storage attributed to diffusion even when the scan rate is increased to 1.0 mV s^{-1}.

To further understand the charge storage mechanism of the Zn-TFB, the GG Zn-TFBs were charged and discharged to different states of charge, and ex situ Raman measurements were performed at each state. This allowed for the monitoring of structural transformations and the morphology of the porous V_2O_5 cathodes during the charge/discharge process. Figure S10a (Supporting Information) shows the Raman spectra of the porous V_2O_5 cathodes at different states of charge, as displayed in Figure S10b (Supporting Information), where the electrodes were obtained by charging and discharging the porous V_2O_5 cathodes, then disassembled and cleaned for ex situ Raman measurements. At point A, the open circuit voltage remains at 1.06 V without participating in any charge/discharge process. At this stage, Raman peaks are located ≈155 cm^{-1} (V—O—V lattice bending vibration), 269 cm^{-1} (O_3—V═O bond bending vibration), 524 cm^{-1} (V_3—O bond stretching vibration), 701 cm^{-1} (V_2—O bond stretching vibration), and 1005 cm^{-1} (V═O bond stretching vibration). When discharged to point B at 0.2 V, Zn^{2+} intercalates into V_2O_5 to form $Zn_xV_2O_5{\cdot}nH_2O$, reducing the crystallinity of V_2O_5 and causing a decrease in the intensity of all peaks compared to point A. As the cathode is gradually charged to point D at 1.6 V through point C at 1.06 V, Zn^{2+} is slowly extracted from $Zn_xV_2O_5{\cdot}nH_2O$ to form V_2O_5. The intensity of the Raman peaks increases progressively from point B to point D. During discharging to points E and F, the peak intensity decreases again, consistent with the reversible storage of Zn^{2+} in the V_2O_5 material. The gradual emergence and fading of the Raman peaks clearly signify the extraction and intercalation of Zn^{2+} ions, as noted in previous studies.[31,32] Figure S10c–h (Supporting Information) shows SEM images of the cathodes at various states of charge, all exhibiting the expected nanosheet-like morphology. Additionally,

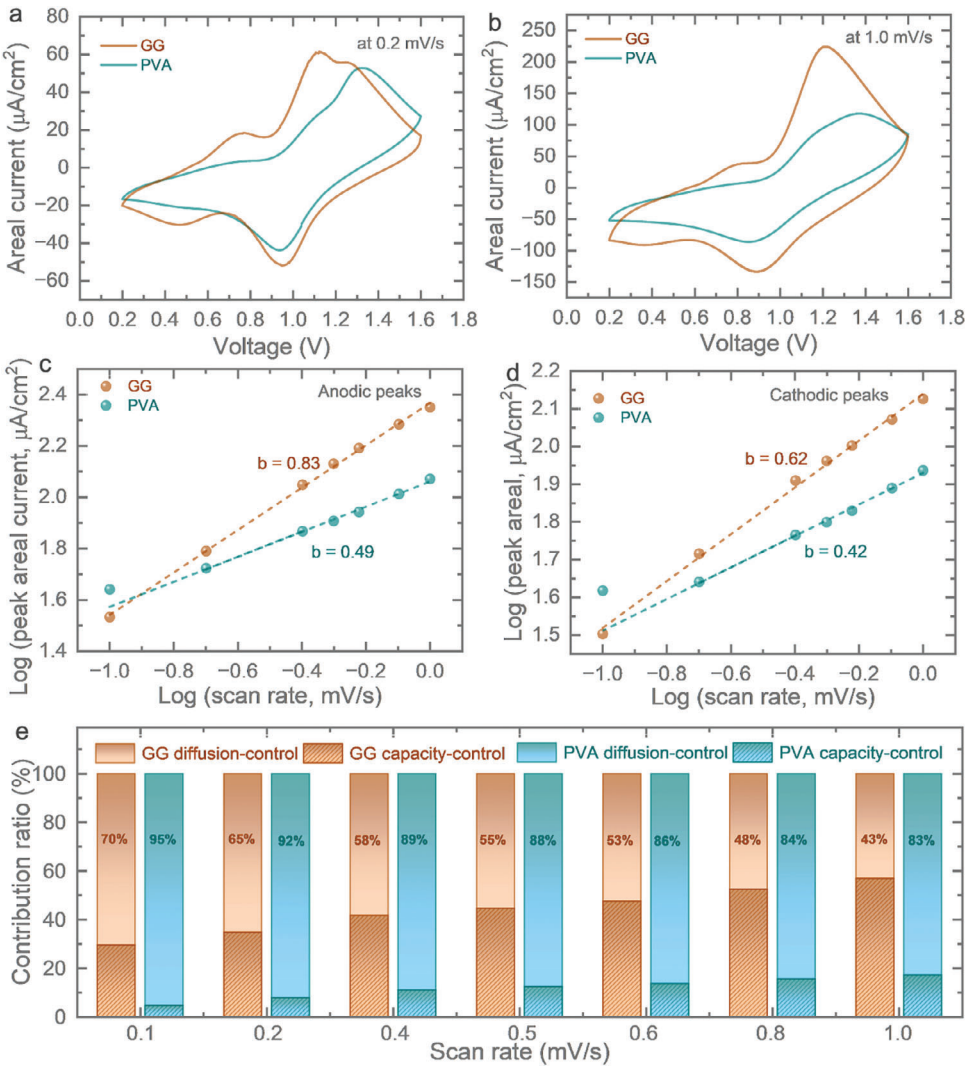

Figure 2. a,b) Comparative CVs of GG and PVA Zn-TFBs at scan rates of 0.2 and 1.0 mV s^{-1} over a voltage range of 0.2 to 1.6 V. b-value calculations for c) anodic and d) cathodic peaks of the Zn-TFBs. e) Diffusion-controlled and capacitive-controlled contribution ratios for GG and PVA at different scan rates ranging from 0.1 to 1.0 mV s^{-1}.

to assess the flexibility of the porous V_2O_5 cathodes, we bent the cathodes to 30° and 70° and captured SEM images after bending, as shown in Figure S11 (Supporting Information). Notably, no distinct cracks appeared on the porous V_2O_5 surface, even after bending to 30° or 70°, indicating that the porous V_2O_5 thin-film cathodes in the Zn-TFBs possess good crimping flexibility.

Additionally, we have conducted extended GDC tests for the GG and PVA Zn-TFBs at different areal currents ranging from 50 to 1000 μA cm^{-2} over the same voltage window of 0.2 to 1.6 V, as tested in the CVs. Figure S8c,d (Supporting Information) displays the GDCs at different areal currents for GG and PVA Zn-TFBs. As expected from the CV tests, the GG Zn-TFBs show higher areal capacities compared to PVA, even at the same areal currents. The comparative GDCs at 50 μA cm^{-2} (**Figure 3a**) and 1000 μA cm^{-2} (Figure 3b) clearly demonstrate higher areal capacities when Zn-TFBs are tested in GG electrolyte compared to PVA. At 50 μA cm^{-2}, the measured areal capacities are 47.34 and 30.18 μAh cm^{-2} in GG and PVA, respectively, while at 1000 μA cm^{-2}, the values are 12.10 and 5.87 μAh cm^{-2}. Further rate tests (Figure 3c) clearly show that Zn-TFBs tested with GG exhibit higher areal capacities than those tested with PVA. As the areal current increases from 50 to 100, 200, 500, and 1000 μA cm^{-2}, the areal capacity of GG decreases from ≈47 to 34, 27, 18, and 12 μAh cm^{-2}, respectively. In comparison, PVA's areal capacity drops from ≈30 to 20, 13, 8, and 6 μAh cm^{-2}. When the areal current is reduced stepwise back to 50 μA cm^{-2}, GG's capacity fully recovers, while PVA's areal capacity only restores to 26 μAh cm^{-2}, indicating a capacity retention of 87%.

To further understand the enhanced capacities of Zn-TFBs tested with GG compared to PVA, we first conducted conductivity tests on the GG and PVA gel electrolytes by fabricating coin cells with stainless steel (SS) symmetric current collectors and performing extended EIS tests at various temperatures, ranging from 25 to 65 °C. Figure S12a,b (Supporting Information) displays the Nyquist plots at different temperatures for GG and PVA, respectively. It is observed that GG exhibits higher

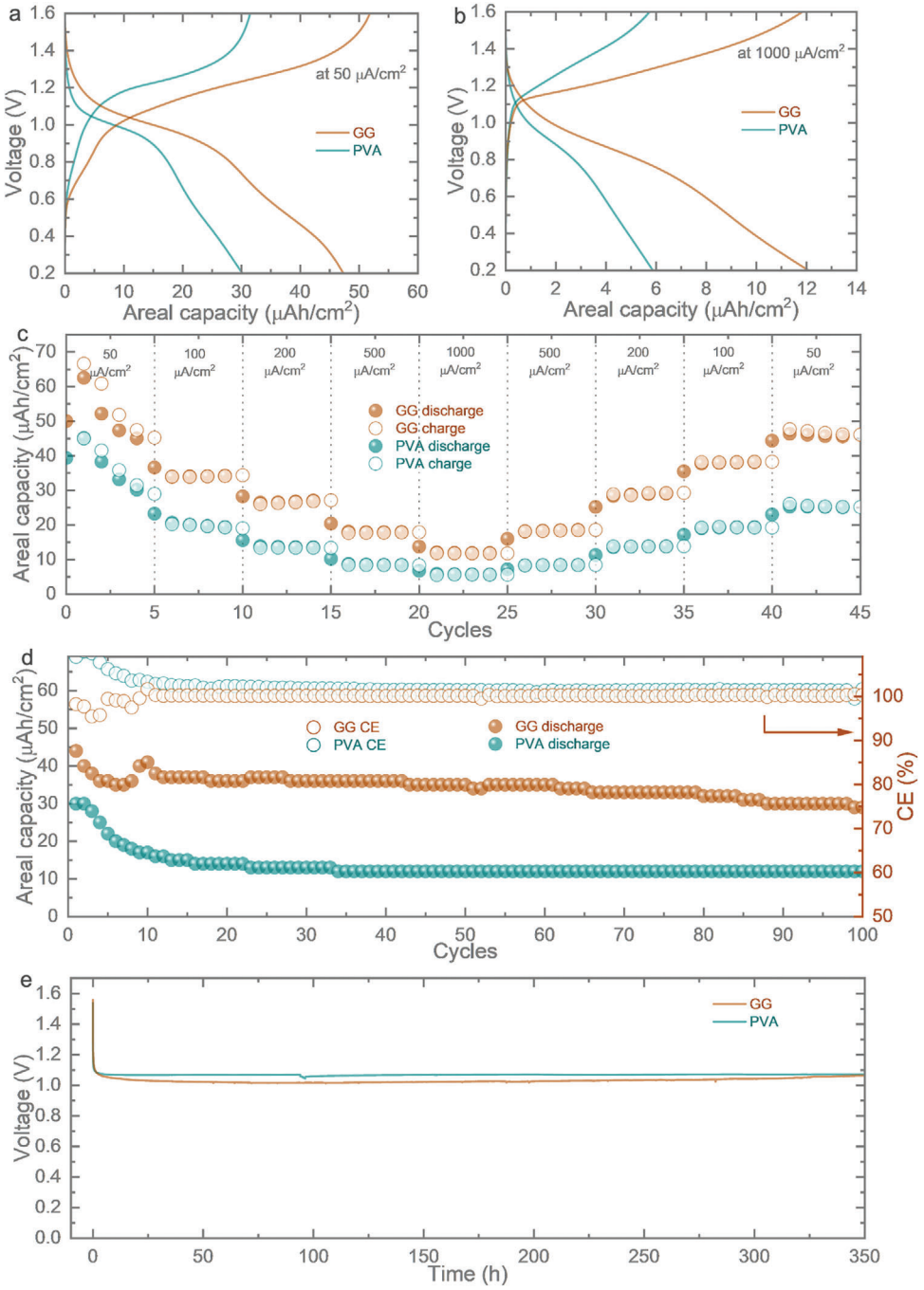

Figure 3. Comparative GDCs of GG and PVA Zn-TFBs at areal currents of a) 50 μA cm^{-2} and b) 1000 μA cm^{-2}. c) Rate capability (from 50 to 1000 μA cm^{-2}, then back to 50 μA cm^{-2}). d) Extended cycling performance of GG and PVA Zn-TFBs. e) Self-discharge performance of GG and PVA Zn-TFBs over 350 h.

ionic conductivity (≈11.30 mS cm^{-1} at 35 °C) compared to PVA (7.89 mS cm^{-1} at 35 °C). Tables S2 and S3 (Supporting Information) present the ionic conductivities at different temperatures, with GG showing superior ionic conductivity compared to PVA across all temperatures. To better understand the higher ionic conductivities observed in GG compared to PVA, we extended our testing to evaluate the viscosities of both GG and PVA gel electrolytes. The viscosities, measured using a viscometer, were 1.25 P for GG (Figure S13a, Supporting Information) and 1.59 P for PVA (Figure S13b, Supporting Information) at 50 °C. Since higher viscosity increases the energy required for Zn^{2+} ion transfer, it results in lower ionic conductivity in PVA gel electrolytes compared to GG. This improved conductivity likely contributes to the enhanced charge storage performance in GG compared to PVA. Additionally, to examine Zn^{2+} plating and stripping behaviors in GG and PVA gel electrolytes and their

corresponding activation energies, we assembled symmetric Zn//Zn cells and tested them using EIS at different temperatures. The corresponding Nyquist plots are shown in Figure S14a,b (Supporting Information). Based on the Arrhenius plots, the calculated activation energies are 48.1 and 55.6 kJ mol^{-1} for GG and PVA, respectively (Figure S14c, Supporting Information). This further confirms that the cells with GG, having a lower activation energy, require less energy to initiate a redox reaction. This implies faster Zn^{2+} diffusion or desolvation between the electrolyte and the zinc electrode. It is important to note that the overall charge storage performance in ZIBs is not solely influenced by the cathode but also by the anode material. Previous studies have shown that dendrite-suppressing zinc anodes with lower activation energies demonstrate better charge storage performance compared to pristine zinc anodes with higher activation energies, even when tested in full cells with similar cathodes.[33] Furthermore, the Nyquist plots of GG and PVA Zn-TFBs, shown in Figure S15a (Supporting Information), indicate that the charge transfer resistance is lower in GG compared to PVA, suggesting that GG electrolytes have better charge transfer kinetics. As a result, the combination of higher ionic conductivity, lower activation energy, and reduced charge transfer resistance in GG compared to PVA leads to superior charge storage performance in GG electrolytes. We also extended our analysis by estimating the relative change in Zn^{2+} ion diffusion coefficients, where the real impedance is related to the diffusion coefficient. The formula used is: $Re(Z) = (R_L + R_D) + \sigma\omega^{-0.5}$ and $D_{zn^{2+}} = \frac{R^2T^2}{2A^2n^4F^4C^2\sigma^2} = \frac{K}{\sigma^2}$; where $(R_L + R_D)$ represents the total resistance from both the solution and charge transfer, σ is the Warburg coefficient, ω is the angular frequency, and $Re(Z)$ is the real impedance extracted from the Nyquist plot. $D_{zn^{2+}}$ ($cm^2\ s^{-1}$) denotes the diffusion coefficient of Zn^{2+} ions, R (8.314 J K^{-1} mol^{-1}) is the molar gas constant, T (298.13 K) is the temperature during testing, n is the number of electrons transferred per unit of the polymer electrolyte, A (cm^2) is the active electrode surface area, F (96485.3383 C mol^{-1}) is Faraday's constant, and C is the concentration of Zn^{2+} ions in the electrolyte. Since the electrode surface area and Zn^{2+} ion concentration are identical, the constant $K = \frac{R^2T^2}{2A^2n^4F^4C^2}$ is the same for both GG and PVA Zn-TFBs. Using this relationship, we calculated the slopes from the $Re(Z)$ versus $\omega^{-0.5}$ graph shown in Figure S15b (Supporting Information). The lower slope for the GG Zn-TFB indicates a higher Zn^{2+} ion diffusion coefficient than that observed in the PVA Zn-TFB.[34]

Figure 3d presents the extended cycling performance of GG and PVA Zn-TFBs over 100 cycles. After the initial 10 cycles, GG's capacity gradually decreases to 30 μAh cm^{-2} by the 100th cycle, retaining 68% of its initial capacity. In contrast, PVA's capacity drops to 12 μAh cm^{-2} within the first 35 cycles and remains at that level for the remainder of the cycles, indicating that GG exhibits better capacity retention than PVA. Additionally, both thin-film batteries maintain 100% Coulombic efficiency at the 100th cycle. Therefore, Zn-TFBs based on GG not only offer higher capacities but also demonstrate better cycling stability compared to those tested in PVA gel electrolytes. Moreover, self-discharge tests are essential for evaluating battery performance, and we extended our studies to examine the self-discharge behavior of both GG and PVA Zn-TFBs after charging them to 1.6 V (Figure 3e). In these tests, GG and PVA were charged to the maximum voltage of

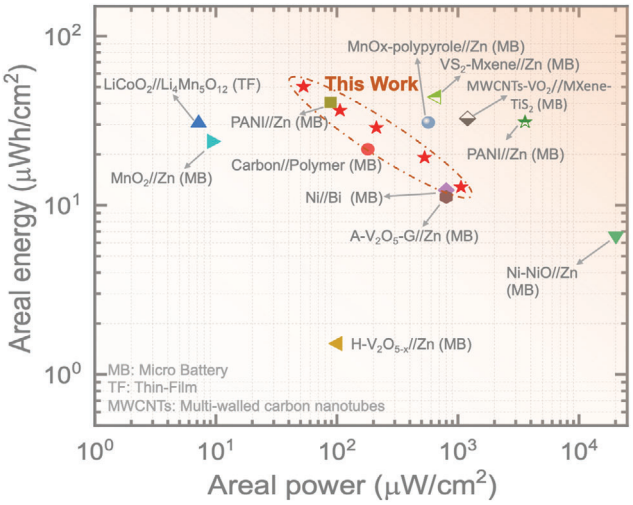

Figure 4. Ragone plot of GG Zn-TFB, comparing the areal energies and areal powers with reported high-performance thin-film batteries: L-V_2O_5//Zn,[6] $LiCo_2O_4$//$Li_4Mn_5O_{12}$,[43] and micro-batteries: Ni-NiO//Zn,[49] A-V_2O_5-G//Zn,[40] Ni//Bi,[44] Carbon//Polymer,[42] MnO_2//Zn,[39] PANI//Zn,[41] 3D Au PANI//Zn,[48] MWCNT-VO_2//MXene-TiS_2,[47] VS_2-MXene//Zn,[45] MnOx-polypyrole//Zn.[46]

1.6 V with an areal current of 100 μA cm^{-2}. The changes in their open-circuit voltage were then monitored over time. Remarkably, both GG and PVA were able to maintain their OCVs at 1.06 and 1.07 V, respectively, for more than 350 h, showing a voltage reduction of less than 34%. This level of voltage retention exceeds that of previously reported planar energy storage micro-devices. For instance, a 50% voltage reduction was observed within 3 h in a Fe-MnO_2 symmetric micro-supercapacitor.[35] AC-based symmetric micro-supercapacitors showed a 50% voltage drop after 2.5 h.[36] A laser-written GO film-based symmetric micro-supercapacitor took 13 h to experience a 50% voltage drop,[37] while laser-written rGO-based symmetric micro-supercapacitors showed a 50% voltage reduction in less than 1 h.[38]

Additionally, we extended the calculations of the areal energies and areal powers of the GG Zn-TFBs and compared the results with reported thin-film batteries and planar micro-batteries in a Ragone plot (**Figure 4**). The calculated areal energies are ≈50.18, 32.29, 28.69, 19.18, and 12.80 μWh cm^{-2}, corresponding to areal powers of 53, 106, 212, 530, and 1060 μW cm^{-2}. These performances surpass many reported micro-batteries and thin-film batteries, such as MnO_2//Zn,[39] H-V_2O_5-X//Zn,[6] A-V_2O_5/G//Zn,[40] PANI//Zn,[41] Carbon//Polymer,[42] $LiCoO_2$//$Li_4Mn_5O_{12}$[43] and Ni//Bi.[44] Though they are slightly lower than some high-performance micro-batteries for instance, VS_2-Mxene//Zn,[45] MnO_x-polypyrole//Zn,[46] MWCNT-VO_2//Mxene-TiS_2,[47] 3D Au PANI//Zn[48] and Ni-NiO//Zn.[49] However, our thin-film cathode preparation, processing, and device fabrication are straightforward and efficient. This highlights the potential of our work, particularly in the fabrication of high-quality porous V_2O_5 thin-films using an industry-viable spray technique. To further demonstrate the practical usability of our GG Zn-TFBs, we extended the tests to power commercial electronic devices by connecting two Zn-TFBs in series. The CVs

and GCDs for both series and parallel configurations are provided in the Supporting Information (Figure S16, Supporting Information). Parallel integration increased the current in the CV graph and prolonged the discharge time in the GCD graph. Series integration doubled the voltage range from 0.2–1.6 to 0.2–3.0 V. These results demonstrate that various currents, discharge times, and voltages can be achieved by assembling GG cells in different configurations. For instance, two GG Zn-TFBs connected in series were able to power both a red LED and an indoor and outdoor thermometer. It was observed that the two GG Zn-TFBs could effectively power the red LED and the indoor and outdoor thermometer. Figure S16c–f (Supporting Information) displays digital images of the red LED and the Indoor and Outdoor Thermometer with Hygrometer Clock being continuously powered for 90 min. To further understand the advantages of our porous V_2O_5 thin-film cathodes compared to the V_2O_5 thin-film cathode prepared by physical vapor deposition (PVD) sputtering, we tested and compared the results using CV and GCD curves, as shown in Figure S17 (Supporting Information). It should be noted that obtaining porous V_2O_5 through the PVD technique is challenging, as indicated in Figure S17a (Supporting Information), potentially limiting the overall capacity in the electrode area of Zn-TFBs. As expected, the chemically processed porous V_2O_5 Zn-TFBs exhibit much higher charge storage performance than the V_2O_5 cathodes produced by the sputtering technique. This leads to the conclusion that the porous structure of the V_2O_5 thin-film offers several benefits, including an increased number of active sites, an enhanced electrolyte-electrode interface, expanded surface area, and improved electrolyte ion diffusion. These factors together lead to superior charge storage performance in porous V_2O_5 compared to V_2O_5 thin-film cathodes produced by the PVD process.

3. Conclusion

To conclude, this study presents a scalable and efficient chemical process for producing porous V_2O_5 thin-films aimed at enhancing the performance of Zn-TFBs. The porous structure of the V_2O_5 thin-film brings several advantages: it promotes efficient interaction between the electrolyte and the electrode, increases the number of active sites, improves the electrolyte-electrode interface, expands the surface area, and allows for better electrolyte ion diffusion. These factors together result in enhanced charge storage capacity when using guar gum gel electrolytes. The Zn-TFBs developed in this study exhibit remarkable charge storage characteristics, with an areal capacity of 47.34 μAh cm^{-2}, an areal energy of 50.18 μWh cm^{-2}, and an areal power of 53 μW cm^{-2} at an areal current of 50 μA cm^{-2}, surpassing many existing microbatteries and thin-film batteries. Overall, this research introduces a cost-effective, scalable, and industry-friendly method for creating highly porous thin-film cathodes, paving the way for the production of high-performance, affordable, and safer thin-film batteries.

Supporting Information

Supporting Information is available from the Wiley Online Library or from the author.

Acknowledgements

B.D.B. acknowledges support from the EPSRC research grant EP/Y008103/1. M.J.C is thankful for the financial support from the China Scholarship Council (No. 202308320319).

Conflict of Interest

The authors declare no conflict of interest.

Data Availability Statement

The data that support the findings of this study are available from the corresponding author upon reasonable request.

Keywords

chemically process, high-performance, V_2O_5 thin-film, zinc-ion thin-film batteries

Received: September 19, 2024
Revised: October 21, 2024
Published online:

[1] P. He, Y. Zhou, X. Qin, *Future Internet* **2024**, *16*, 128.
[2] Y. Yang, W. Gao, *Chem. Soc. Rev.* **2019**, *48*, 1465.
[3] P. Li, M. Liao, J. Li, L. Ye, X. Cheng, B. Wang, H. Peng, *Small Struct.* **2022**, *3*, 2200058.
[4] M. Wakihara, *Mater. Sci. Eng.: R: Rep.* **2001**, *33*, 109.
[5] M. Zheng, H. Tang, Q. Hu, S. Zheng, L. Li, J. Xu, H. Pang, *Adv. Funct. Mater.* **2018**, *28*, 1707500.
[6] S. H. Cho, J. S. Park, J. H. Kim, Y. H. Chang, J. Ahn, J. S. Nam, J. W. Jung, I. D. Kim, H. S. Kim, *ACS Appl. Energy Mater.* **2023**, *6*, 2719.
[7] C. Yin, C. Pan, X. Liao, Y. Pan, L. Yuan, *ACS Appl. Mater. Interfaces* **2021**, *13*, 35837.
[8] S. Xie, X. Li, Y. Li, Q. Liang, L. Dong, *Chem. Rec.* **2022**, *22*, 202200201.
[9] X. Xu, Y. Chen, D. Liu, D. Zheng, X. Dai, W. Shi, X. Cao, *Chem. Rec.* **2022**, *22*, 202200079.
[10] M. Li, M. Maisuradze, R. Sciacca, I. Hasa, M. Giorgetti, *Batter. Supercaps* **2023**, *6*, 202300340.
[11] W. Zhang, C. Zuo, C. Tang, W. Tang, B. Lan, X. Fu, S. Dong, P. Luo, *Energy Technol.* **2020**, *9*, 2000789.
[12] V. Mathew, B. Sambandam, S. Kim, S. Kim, S. Park, S. Lee, M. H. Alfaruqi, V. Soundharrajan, S. Islam, D. Y. Putro, J. Y. Hwang, Y. K. Sun, J. Kim, *ACS Energy Lett.* **2020**, *5*, 2376.
[13] X. Wang, L. Wang, B. Zhang, J. Feng, J. Zhang, X. Ou, F. Hou, J. Liang, *J. Energy Chem.* **2021**, *59*, 126.
[14] Y. Lu, Y. Wen, F. Huang, T. Zhu, S. Sun, B. C. Benicewicz, K. Huang, *Energy Storage Mater.* **2020**, *27*, 418.
[15] T. M. McFarlane, J. A. Shetzline, S. Creager, C. F. Huebner, C. Tonkin, S. Foulger, *J. Mater. Chem. A* **2017**, *5*, 6432.
[16] A. H. Seikh, *Trans. Indian Inst. Met.* **2021**, *75*, 193.
[17] M. Jayachandran, A. Rose, T. Maiyalagan, N. Poongodi, T. Vijayakumar, *J. Mater. Sci.: Mater. Electron.* **2021**, *32*, 6623.
[18] D. S. Charles, X. Teng, *Alkali-Ion Batteries*, InTech, London, UK **2016**.
[19] D. Vernardou, *Adv. Mater. Lett.* **2013**, *4*, 798.
[20] H. Qin, L. Chen, L. Wang, X. Chen, Z. Yang, *Electrochim. Acta* **2019**, *306*, 307.
[21] Q. He, H. Wang, J. Bai, Y. Liao, S. Wang, L. Chen, *J. Colloid Interface Sci.* **2024**, *662*, 490.

[22] D. Zhao, X. Wang, W. Zhang, Y. Zhang, Y. Lei, X. Huang, Q. Zhu, J. Liu, *Adv. Funct. Mater.* **2023**, *33*, 2211412.
[23] Z. Feng, J. Sun, Y. Liu, H. Jiang, T. Hu, M. Cui, F. Tian, C. Meng, Y. Zhang, *J. Power Sources* **2022**, *536*, 231489.
[24] F. Liang, M. Chen, S. Zhang, Z. Zou, C. Ge, S. Jia, S. Le, F. Yu, J. Nong, *ACS Sustainable Chem. Eng.* **2024**, *12*, 5117.
[25] A. Kumar, P. P. Sahay, *J. Sol-Gel Sci. Technol.* **2020**, *95*, 34.
[26] I. J. Tadeo, R. Parasuraman, A. M. Umarji, *Sens. Actuators, B* **2021**, *337*, 129811.
[27] S. Luo, J. Cui, S. Liang, Y. Guo, B. Yuan, L. Xu, R. Zheng, J. Li, W. Yang, M. Chen, Y. Lu, Y. Luo, *ACS Appl. Nano Mater.* **2024**, *7*, 1655.
[28] G. Silversmit, D. Depla, H. Poelman, G. B. Marin, R. De Gryse, *J. Electron Spectrosc. Relat. Phenom.* **2004**, *135*, 167.
[29] B. D. Boruah, A. Mathieson, S. K. Park, X. Zhang, B. Wen, L. Tan, A. Boies, M. D. Volder, *Adv. Energy Mater.* **2021**, *11*, 2100115.
[30] T. Yang, D. Xin, N. Zhang, J. Li, X. Zhang, L. Dang, Q. Li, J. Sun, X. He, R. Jiang, Z. Liu, Z. Lei, *J. Mater. Chem. A* **2024**, *12*, 10137.
[31] M. S. Javed, H. Lei, Z. Wang, B. Liu, X. Cai, W. Mai, *Nano Energy* **2020**, *70*, 104573.
[32] F. Ming, H. Liang, Y. Lei, S. Kandambeth, M. Eddaoudi, H. N. Alshareef, *ACS Energy Lett.* **2018**, *3*, 2602.
[33] X. Hu, J. Borowiec, Y. Zhu, X. Liu, R. Wu, A. M. Ganose, I. P. Parkin, B. D. Boruah, *Small* **2023**, *20*, 2306827.
[34] Y. Zhu, N. Naresh, X. Liu, J. Luo, Y. Fan, M. Cao, B. Li, M. Wang, B. D. Boruah, *Small* **2024**, 2405733
[35] Y. Wang, Y. Z. Zhang, Y. Q. Gao, G. Sheng, J. E. T. Elshof, *Nano Energy* **2020**, *68*, 104306.
[36] C. Gao, J. Huang, Y. Xiao, G. Zhang, C. Dai, Z. Li, Y. Zhao, L. Jiang, L. Qu, *Nat. Commun.* **2021**, *12*, 2647.
[37] M. F. El-Kady, R. B. Kaner, *Nat. Commun.* **2013**, *4*, 1475.
[38] W. Gao, N. Singh, L. Song, Z. Liu, A. L. M. Reddy, L. Ci, R. Vajtai, Q. Zhang, B. Wei, P. M. Ajayan, *Nat. Nanotechnol.* **2011**, *6*, 496.
[39] X. Wang, S. Zheng, F. Zhou, J. Qin, X. Shi, S. Wang, C. Sun, X. Bao, Z. S. Wu, *Natl. Sci. Rev.* **2019**, *7*, 64.
[40] X. Wang, Y. Li, S. Wang, F. Zhou, P. Das, C. Sun, S. Zheng, Z. Wu, *Adv. Energy Mater.* **2020**, *10*, 2000081.
[41] S. Bi, F. Wan, S. Huang, X. Wang, Z. Niu, *ChemElectroChem* **2019**, *6*, 3933.
[42] H. S. Min, B. Y. Park, L. Taherabadi, C. Wang, Y. Yeh, R. Zaouk, M. J. Madou, B. Dunn, *J. Power Sources* **2008**, *178*, 795.
[43] M. Kotobuki, Y. Suzuki, H. Munakata, K. Kanamura, Y. Sato, K. Yamamoto, T. Yoshida, *Electrochim. Acta* **2011**, *56*, 1023.
[44] L. He, T. Hong, X. Hong, X. Liao, Y. Chen, W. Zhang, H. Liu, W. Luo, L. Mai, *Energy Technol.* **2019**, *7*, 1900144.
[45] Y. Feng, Y. Feng, Y. Zhang, L. Sun, X. Li, M. Meng, Y. Zhu, K. Liu, *J. Power Sources* **2022**, *545*, 231944.
[46] M. Zhu, Z. Wang, H. Li, Y. Xiong, Z. Liu, Z. Tang, Y. Huang, A. L. Rogach, C. Zhi, *Energy Environ. Sci.* **2018**, *11*, 2414.
[47] B. Zhao, S. Wang, Q. Yu, Q. Wang, M. Wang, T. Ni, L. Ruan, W. Zeng, *J. Power Sources* **2021**, *504*, 230076.
[48] N. Naresh, Y. Zhu, J. Luo, Y. Fan, T. Wang, K. Raju, M. De Volder, I. P. Parkin, B. D. Boruah, *Adv. Funct. Mater.* **2024**, 2413777.
[49] Y. Zeng, Y. Meng, Z. Lai, X. Zhang, M. Yu, P. Fang, M. Wu, Y. Tong, X. Lu, *Adv. Mater.* **2017**, *29*, 1702698.